Computational Study of Nose Bluntness Effects for Spinning Shells at Supersonic Speeds

Walter B. Sturek,* Bernard Guidos,† and Charles J. Nietubicz‡
U.S. Army Ballistic Research Laboratory, ARRADCOM, Aberdeen Proving Ground, Maryland

Recent papers have reported the application of the thin-layer parabolized Navier-Stokes (PNS) computational technique to predict the Magnus effect for spinning, sharp-tipped shell at supersonic speeds. This paper reports the results of a computational study in which the time-marching, thin-layer Navier-Stokes computational technique is used to generate a starting solution for hemisphere and flattened blunt-nose configurations and the PNS code is used to compute the flow over the remainder of the shell. Results have been obtained for $1.5 < M < 5$ for sharp, hemisphere, and flattened nose configurations. The Magnus effect for the small nose bluntness typical of Army shell is found to be 15% greater for the hemisphere nose shell than for the sharp nose configuration at $M = 3$.

Nomenclature

a = speed of sound
CP = center of pressure for normal force
CP_Y = center of pressure for Magnus force
C_m = pitching moment coefficient
$C_{M_{p\alpha}}$ = $C_n/[(PD/v)(\alpha)]$, slope of Magnus moment coefficient evaluated at $PD/V = 0$, $\alpha = 0$
C_n = Magnus (yawing) moment coefficient
C_N = normal force coefficient
C_Y = Magnus (side) force
D = diameter of model
e = total energy per unit volume of fluid, normalized by $\rho_\infty a_\infty{}^2$
$\hat{E}, \hat{E}_s, \hat{F}, \hat{G}$ = flux vectors of transformed gasdynamic equation
J = Jacobian of transformation between physical and computational coordinates
L = reference length
M = Mach number
p = pressure normalized by $\rho_\infty a_\infty{}^2$
Pr = Prandtl number, $\mu_\infty c_p/\kappa_\infty$
PD/V = nondimensional spin rate about model axis
$\hat{R}e$ = Reynolds number, $\rho_\infty a_\infty L/\mu_\infty$
$\hat{S}$ = viscous flux vector
u, v, w = Cartesian velocity components along x, y, z, axes, respectively, normalized by a_∞
U, V, W = contravariant velocity components
x, y, z = physical Cartesian coordinate axis
α = angle of attack
γ = ratio of specific heats
κ = coefficient of thermal conductivity, normalized by freestream value κ_∞
μ = coefficient of viscosity, normalized by freestream value μ_∞
ξ, η, ζ = computational coordinates in the axial, circumferential, and radial directions
ρ = density, normalized by freestream density ρ_∞

Subscripts

∞ = freestream conditions
w = body surface values
x = based on axial distance from nose

I. Introduction

RECENT papers[1-4] have reported the development and application of the thin-layer, parabolized Navier-Stokes (PNS) computational technique to predict the flow about slender bodies of revolution with sharp noses at supersonic velocities. Reference 3 showed the technique to be a viable computational tool for predicting the Magnus effect for a six-caliber slender shell with a one-caliber, 7-deg boattail as verified by comparison to wind tunnel force measurements. Reference 4 reported the results of applying the PNS computational technique to determine the Magnus effect and other aerodynamic coefficients for a parametric variation in boattail geometry. These computations were all performed for shell with sharp tips. This paper reports a computational study of the influence of nose bluntness on the Magnus effect of shell using a starting solution generated by the unsteady Navier-Stokes (time-marching) computational technique and then using the PNS (space-marching) code to compute the flow over the remainder of the shell.

A spark shadowgraph of an artillery shell at a velocity of approximately $M = 2.25$ taken in the BRL Transonic Range is shown in Fig. 1. This shadowgraph shows the detached bow shock that occurs for supersonic flow over the artillery shell. Note the presence of a shock at the sharp corner of the flattened nose. This shock is caused by the local flow separation that is induced by the strong expansion at the sharp corner.

A recent wind tunnel test[5] was performed in which aerodynamic force measurements were made for spinning models with sharp, hemisphere, and flattened nose tips. A schlieren photograph of the flow over these nose tips at $M = 3$ is shown in Fig. 2. It is obvious that the bow shock pattern is different for each of these configurations. The inner shock at the nose tip that is very distinct in Fig. 1 also occurs at the sharp corner of the flattened nose in Fig. 2. This shock is not visible for the hemisphere nose. The shock waves starting about 1 diameter downstream of the model nose are generated by a boundary-layer trip.

The purpose of this study is to examine the significance of the technique for modeling the nose region of spinning shell on the predicted aerodynamic behavior at supersonic velocities.

Presented as Paper 82-1341 at the AIAA 9th Atmospheric Flight Mechanics Conference, San Diego, Calif., Aug 9-11, 1982; submitted Aug. 10, 1982; revision received April 6, 1983.

*Chief, Aerodynamics Research Branch. Associate Fellow AIAA.

†Engineer Trainee.

‡Aerospace Engineer. Member AIAA.

II. Computational Techniques

A. Blunt-Nose Solution

The solution for the flow over the blunt nose of the shell has been obtained using the three-dimensional, thin-layer Navier-Stokes solver recently reported by Chaussee, et al.[6] This is a fully implicit computational technique which solves for the entire flowfield by converging to a steadyflow solution. The outer boundary for this code employs a shock-fitting scheme. Since the solution is obtained for only a small flowfield region near the nose, good grid resolution has been achieved. The grid consisted of 30 points from the body to the outer boundary, 20 points axially along the surface of the shell, and 36 points circumferentially around the shell.

The nose region has initially been modeled as a hemisphere cone. The conical extension is of sufficient length to achieve a well-established supersonic conical flow in order to apply the zero gradient outflow boundary condition with confidence. This modeling of the nose region is depicted schematically in Fig. 3. The bluntness ratio is defined to be the ratio of the diameter of the cone at the forward tangency point to the maximum diameter of the shell.

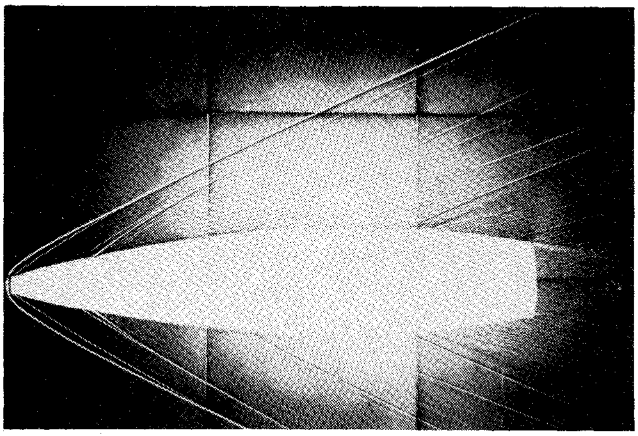

Fig. 1 Aerodynamics range spark shadowgraph of artillery shell at supersonic velocity, $M \approx 2.3$.

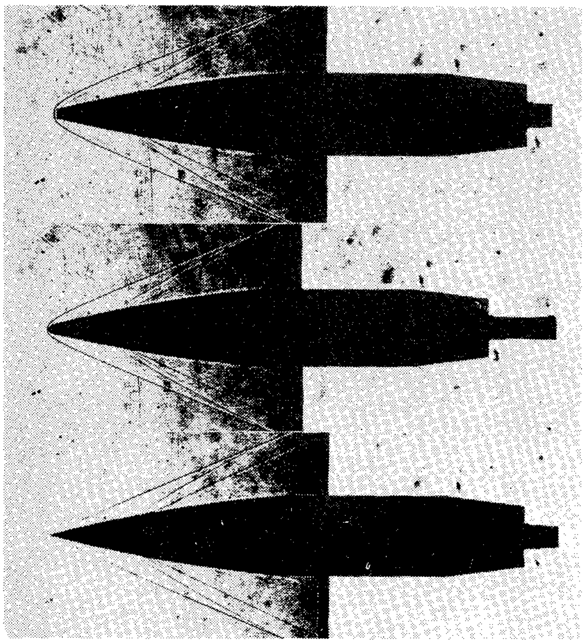

Fig. 2 Schlieren photographs of wind tunnel flow over SOCBT shell with sharp-, hemisphere-, and flattened-nose geometries; $M=3$, $Re=9.19\times10^6/\mathrm{m}$.

In addition to the hemisphere blunt nose, several cases have been run for a flattened nose. The intent is to model as closely as possible the meplate (flat-face) configuration of a typical Army shell.

The time-dependent, thin-layer Navier-Stokes equations can be written in strong conservation-law form as

$$\frac{\partial \hat{q}}{\partial \tau}+\frac{\partial \hat{E}}{\partial \xi}+\frac{\partial \hat{F}}{\partial \eta}+\frac{\partial \hat{G}}{\partial \zeta}=\frac{1}{Re}\frac{\partial \hat{S}}{\partial \zeta} \tag{1}$$

where $\tau=t$ is the time (marching); $\xi=\xi(t, x, y, z)$ the longitudinal coordinate; $\eta=\eta(t, x, y, z)$ the circumferential coordinate; and $\zeta=\zeta(t, x, y, z)$ the near-normal coordinate.

The inviscid flux vectors are $\hat{E}$, $\hat{F}$, $\hat{G}$ are contain terms for the conversation of mass, momentum, and energy in the three coordinate directions. The vector $\hat{q}(\rho, \rho u, \rho v, \rho w, e)$ contains the dependent variables. The $\hat{S}$ matrix contains the viscous terms which are valid for high Reynolds number flows.

The contravariant velocity components are

$$U=\xi_x u+\xi_y v+\xi_z w$$

$$V=\eta_x u+\eta_y v+\eta_z w$$

$$W=\zeta_x u+\zeta_y v+\zeta_z w.$$

Variations of body geometry are included in Eq. (1) through the presence of metric terms (ξ_x, η_x, etc.) and the Jacobian J, which appear in the flux vectors and contravariant velocities. A two-layer algebraic eddy-viscosity model is used for the turbulent viscous solutions.

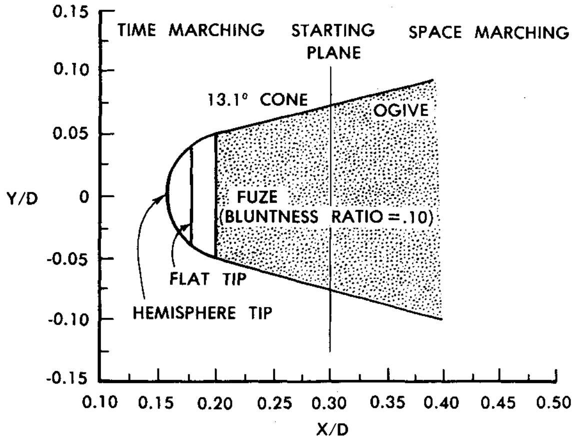

Fig. 3 Blunt-nose tip modeling geometries.

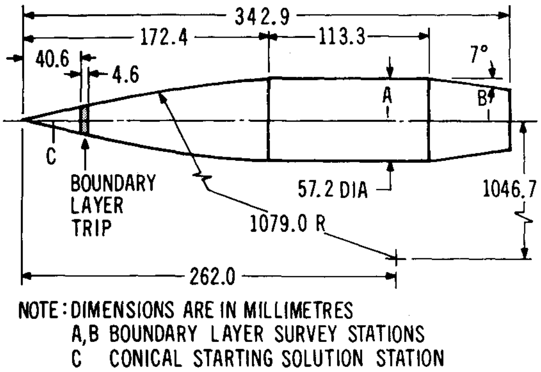

Fig. 4 SOCBT model geometry.

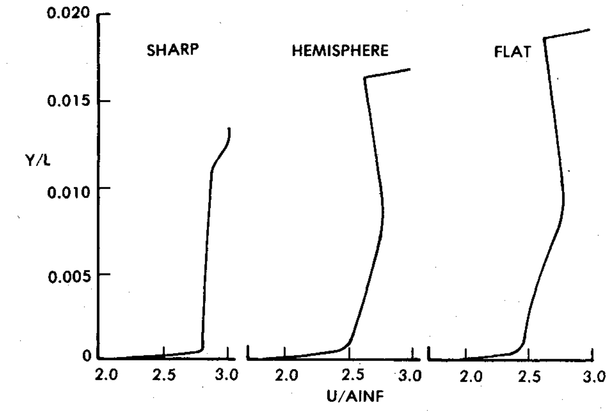

Fig. 5 Leeside u-velocity profiles at starting plane: $M=3$, $\alpha=2$ deg, $PD/V=0.19$; atmospheric flight conditions, $Re=6.80\times10^7$/m.

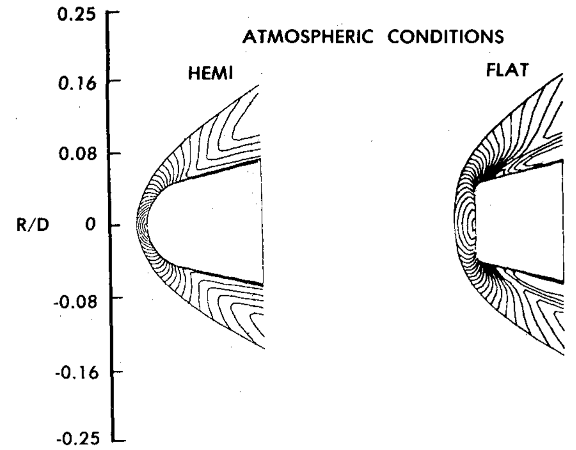

Fig. 6 Mach contours of nose region flow for hemisphere and flattened nose geometries: $M=3$, $\alpha=2$ deg, $PD/V=0.19$; atmospheric flight conditions, $Re=6.80\times10^7$/m.

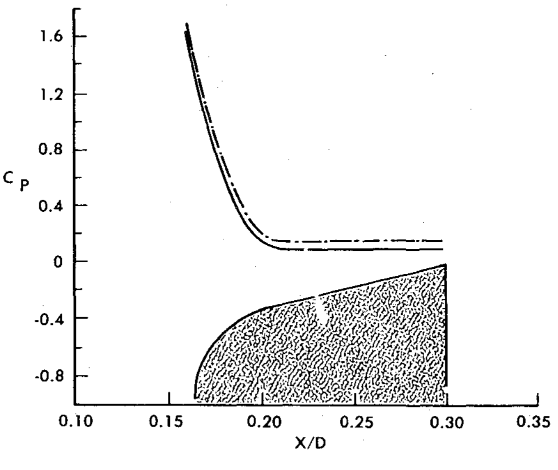

Fig. 7 Surface pressure on hemisphere nose: $M=3$, $\alpha=2$ deg, $PD/V=0.19$; atmospheric flight conditions, $Re=6.80\times10^7$/m.

B. Space-Marching Solution

The thin-layer parabolized Navier-Stokes (PNS) computational technique developed by Schiff and Steger[1] is employed to obtain the flowfield solution downstream from the nose region. The numerical algorithm used in an approximately factored, fully implicit, finite difference scheme. The algorithm is of second-order accuracy in the marching direction. A two-layer algebraic eddy-viscosity model is used for the turbulent viscous solutions. The computational grid

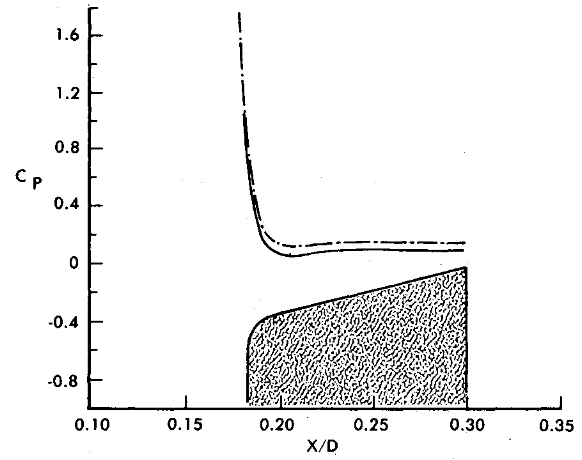

Fig. 8 Surface pressure on flat nose: $M=3$, $\alpha=2$ deg, $PD/V=0.19$; atmospheric flight conditions, $Re=6.80\times10^7$/m.

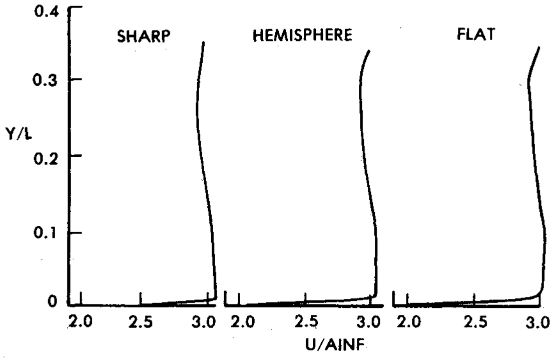

Fig. 9 Leeside u-velocity profiles at $X/D=4.88$, SOCBT model: $M=3$, $\alpha=2$ deg, $PD/V=0.19$; atmosphere flight conditions, $Re=6.80\times10^7$/m.

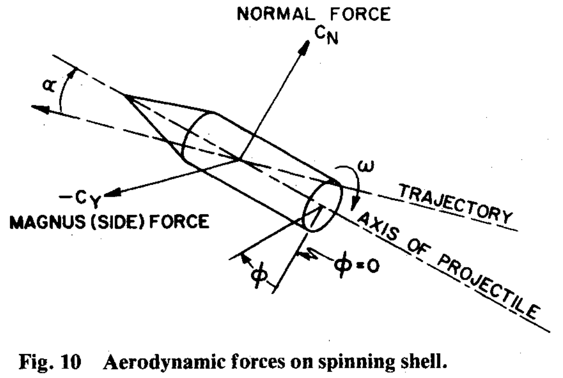

Fig. 10 Aerodynamic forces on spinning shell.

consisted of 36 points at 10 deg intervals circumferentially about the model and 50 points spaced between the body and the outer boundary. A logarithmic stretching is used to achieve adequate grid resolution of the turbulent viscous layer. The streamwise marching step size was adjusted to yield 500 – 800 computational steps for the full length of the shell. The space-marching code uses shock capturing for the outer boundary; no difficulty was experienced in starting the PNS code using the data from the shock-fitted starting solution.

The steady thin-layer Navier-Stokes equations can be written in strong conservation-law form as

$$\frac{\partial \hat{E}_s}{\partial \xi}+\frac{\partial \hat{F}}{\partial \eta}+\frac{\partial \hat{G}}{\partial \zeta}=\frac{1}{Re}\,\frac{\partial \hat{S}}{\partial \zeta} \tag{2}$$

where $\xi=\xi(x)$ is the longitudinal (marching) coordinate;

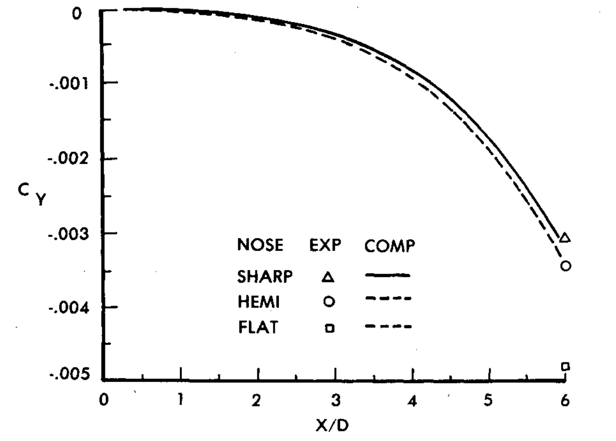

Fig. 11 Magnus force vs axial position, SOCBT model, computation compared to experimental force measurement: $M=3$, $\alpha=2$ deg, $PD/V=0.19$; wind tunnel test conditions, $Re=9.19\times10^6$/m.

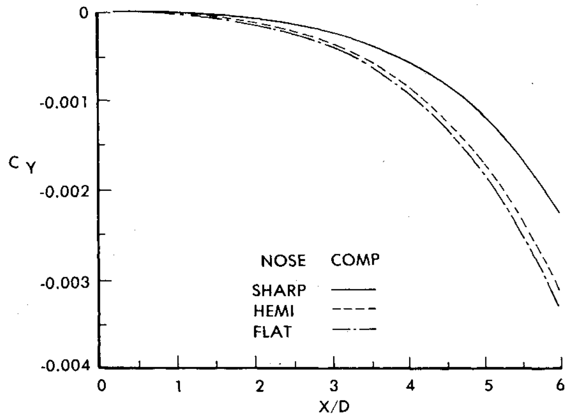

Fig. 12 Magnus force vs axial position, SOCBT model: $M=3$, $\alpha=2$ deg, $PD/V=0.19$; atmospheric flight conditions, $Re=6.80\times10^7$/m.

$\eta=\eta(x,y,z)$ the circumferential coodinate; and $\zeta=\zeta(x,y,z)$ the near-normal coordinate.

The inviscid flux vectors are $\hat{E}_s$, $\hat{F}$, $\hat{G}$ and contain terms for the conservation of mass, momentum, and energy in the three coordinate directions. The vector $\hat{q}(\rho, \rho u, \rho v, \rho w, e)$ contains the dependent variables. The $\hat{S}$ matrix contains the viscous terms which are valid for high Reynolds number flows.

The contravariant velocity components are

$$U=\xi_x u$$

$$V=\eta_x u+\eta_y v+\eta_z w$$

$$W=\zeta_x u+\zeta_y v+\zeta_z w$$

Variations of body geometry are included in Eq. (2) through the presence of metric terms (ξ_x, η_x, ζ_x, etc.) and the Jacobian J, which appear in the flux vectors and contravariant velocities.

III. Results

The model geometry used in this study is the ogive-cylinder-boattail (SOCBT) shape in Fig. 4. Figure 3 shows the nose tip geometries in detail. Flowfield computations have been obtained for wind tunnel test conditions and free-flight atmospheric conditions. The wall temperature boundary condition has been modeled as an adiabatic wall for the wind tunnel tests and as a constant wall temperature equal to the atmospheric temperature for the atmospheric flight conditions.

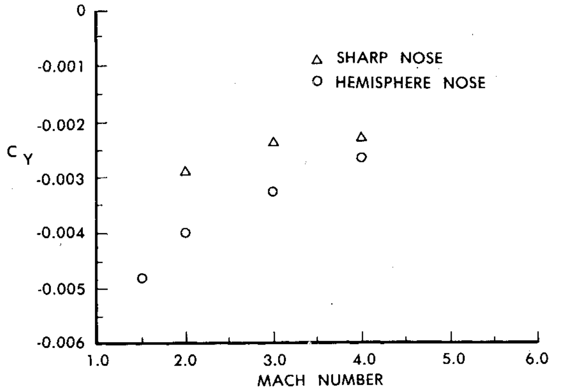

Fig. 13 Magnus force vs Mach number, SOCBT model, comparison between sharp and hemisphere noses; $\alpha=2$ deg, $PD/V=0.19$, atmospheric flight conditions.

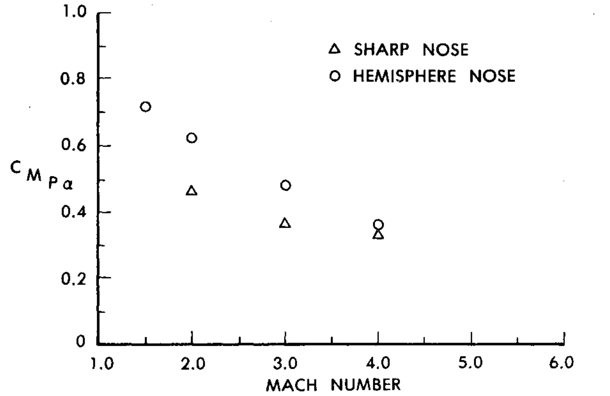

Fig. 14 Slope of Magnus moment coefficient vs Mach number, SOCBT model, comparison between sharp and hemisphere noses, atmospheric flight conditions.

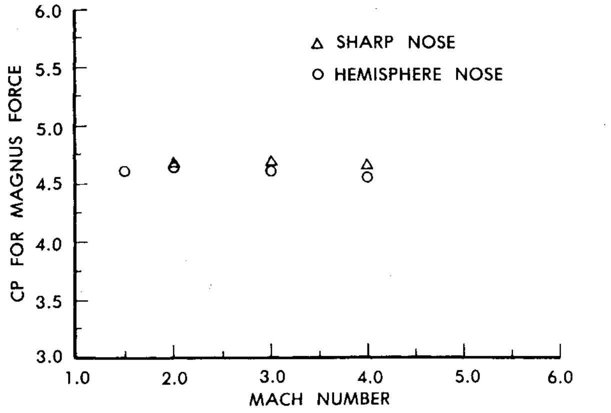

Fig. 15 Magnus force center of pressure vs Mach number, SOCBT model, comparison between sharp and hemisphere noses, atmospheric flight conditions.

Examples of u-velocity profiles at the starting plane for sharp and blunt noses are shown in Fig. 5. The profile for the blunt-nose cases are significantly distorted in the inviscid flow region compared to the sharp-nose case which has a comparatively flat profile. An interesting comparison is shown in Fig. 6, where Mach contours for the blunt starting solutions are shown. The more severe flow expansion around the flattened nose compared to the hemisphere nose is clearly illustrated. Figures 7 and 8 show the distribution of surface pressure for windward and leeward rays for the two nose bluntnesses.

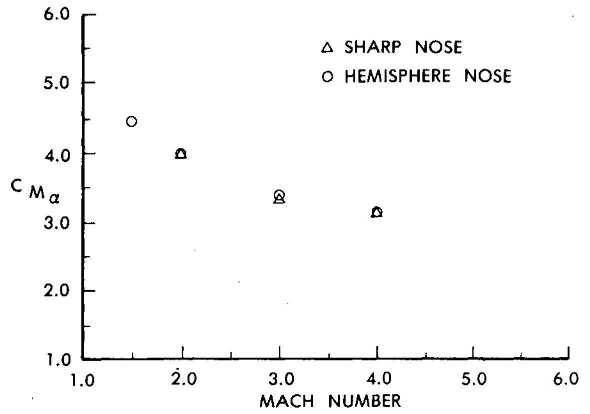

Fig. 16 Slope of pitching moment coefficient vs Mach number, SOCBT model, comparison between sharp and hemisphere noses, atmospheric flight conditions.

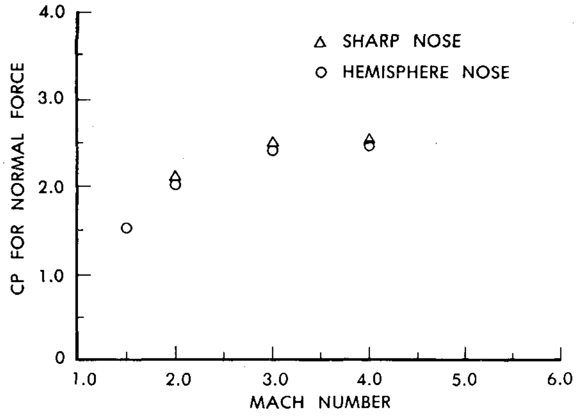

Fig. 17 Normal force center of pressure vs Mach number, SOCBT model, comparison between sharp and hemisphere noses, atmospheric flight conditions.

Additional examples of u-velocity profiles for the different nose configurations are shown in Fig. 9 for a longitudinal station near the start of the boattail. Small but distinct differences are apparent upon comparison of these profiles, indicating that the effect of the initial conditions does not wash out rapidly.

The primary interest in this study is the effect of nose bluntness on the Magnus effect. The sign convention for the aerodynamic forces on a spinning shell is depicted in Fig. 10.

A wind tunnel test[5] was conducted recently to obtain measurements of the aerodynamic forces on a slender shell with sharp, hemisphere, and flattened nose configurations. Force balance measurements were obtained for pitch plane and Magnus forces. Computational results for sharp and hemisphere nose geometries have been obtained for comparison to these data. The computational and experimental results for Magnus force are compared in Fig. 11. The experimental data indicate an increasing Magnus force for increasing nose flatness. The agreement between computation and experiment for the sharp- and hemisphere-nose configurations is quite good. However, there is substantial disagreement between computation and experiment for the flattened nose geometry. The computation for the hemisphere and the flattened nose yielded virtually identical results. This is in sharp contrast to the experimental results which yielded a substantially greater Magnus force for the flat-nose case than that for the hemisphere cap. Further computations, for which the boundary layer on the nose cap was laminar, yielded results that were virtually identical to the results for which the boundary layer on the nose cap was turbulent. A possible cause for the discrepancy is the difference between the flatness of the nose for the computational model and the model used in the wind tunnel test. As shown in Fig. 3, the flat part of the nose does not extend to the full diameter of the meplate. Additional computations are planned in which the actual flatness of the fuze configuration will be modeled more closely. It would also be useful to have experimental data for a wider range of freestream Mach numbers for comparison to the computations.

An example is shown in Fig. 12 of the development of the Magnus force as a function of axial position comparing computational results for sharp-, hemisphere-, and flattened-nose configurations for atmospheric flight conditions. The results indicate a significant increase in the Magnus force for the blunt noses. The trend of increasing Magnus force for increasing nose flattness is observed. Examples of the Magnus force as a function of Mach number for the sharp and hemisphere blunt noses are shown in Fig. 13. The blunt case is consistently greater in absolute magnitude than the sharp case.

The slope of the Magnus moment coefficient as a function of Mach number is shown in Fig. 14 comparing results for sharp and hemisphere noses. Again, the blunt-nose results are consistently greater than those for the sharp nose. The results also predict a greater influence of nose bluntness as the Mach number decreases. The behavior of the Magnus center of pressure is shown in Fig. 15. These results indicate that the Magnus center of pressure is 1) located well downstream of the center of gravity location (3.6 calibers); 2) weakly sensitive to Mach number; and 3) not highly sensitive to the nose bluntness.

The slope of the pitching moment coefficient as a function of Mach number is shown in Fig. 16. These results indicate that the pitching moment moment is not sensitive to small nose bluntness typical of artillery shell. Similarly, the normal force center of pressure (shown in Fig. 17) is also not sensitive to the small nose bluntness considered in this study.

IV. Summary

A computational study has been described in which thin-layer Navier-Stokes computational techniques have been employed to predict the aerodynamics of slender, spinning shell with hemisphere and flattened blunt noses at supersonic velocities. Comparisons have been shown between results obtained in which the nose tip of the shell has been modeled as a sharp cone, a hemisphere cone, and a truncated cone. The results indicate that small nose bluntness, typical of artillery shell, can increase significantly the Magnus moment. The results further indicate that the pitching moment is not strongly affected by the small nose bluntness considered in this study.

References

[1] Schiff, L. B. and Steger, J. L., "Numerical Simulation of Steady Supersonic Viscous Flow," *AIAA Journal*, Vol. 18, Dec. 1980, pp. 1421-1430.

[2] Schiff, L. B. and Sturek, W. B., "Numerical Simulation of Steady Supersonic Flow Over an Ogive-Cylinder-Boattail Body," AIAA Paper 80-0066, Jan. 1980.

[3] Sturek, W. B. and Schiff, L. B., "Numerical Simulation of Steady Supersonic Flow over Spinning Bodies of Revolution," *AIAA Journal*, Vol. 20, Dec. 1982, pp. 1724-1731.

[4] Sturek, W. B., and Mylin, D. C., "Computational Parametric Study of the Magnus Effect of Boattailed Shell at Supersonic Speeds," AIAA Paper 81-1900, Aug. 1981.

[5] Chaussee, D. S., Kutler, P., and Pulliam, T. H., "Three Dimensional Viscous Flow Field Program; Part I: Viscous Blunt Body Program (Interim Report)," AFWL-TM-81-63-FIMG, March 1981.

[6] Unpublished Wind Tunnel Data. Test performed at the Naval Surface Weapons Center, White Oak Laboratory, Silver Spring, Maryland for the U.S. Army Ballistic Research Laboratory, July 1981.